Bulletin of the Seismological Society of America, Vol. 100, No. 1, pp. 207–224, February 2010, doi: 10.1785/0120090105

Ⓔ

Distribution of Seismic Velocities and Attenuation in the Crust beneath the North Anatolian Fault (Turkey) from Local Earthquake Tomography

by I. Koulakov,* D. Bindi, S. Parolai, H. Grosser, and C. Milkereit

Abstract We investigate the crustal structure beneath the western part of the North Anatolian fault zone (NAFZ), an area where at least five damaging earthquakes occurred during the twentieth century. This study is based on local earthquake tomography using the data from aftershocks of the Izmit event (17 August 1999, M 7.4) recorded by stations of permanent and temporary networks. We derive the distribution of V_P, V_S, and the V_P/V_S ratio based on the iterative inversion for both $V_P - V_S$ and $V_P - V_P/V_S$ using the LOTOS code. Innovatively, in this study we perform an inversion for frequency-dependent S-wave attenuation ($1/Q_S$). The reliability of the results is assessed through synthetic tests. The distributions of the resulting seismic parameters (V_P, V_S, V_P/V_S, and Q_S) highlight important geodynamical features in the study area. The low-velocity and high-attenuation patterns mostly correlate with the fracturing zones of the NAFZ. Low velocities are also observed beneath the main sedimentary basins (e.g., Adapazarı, Düzce, and Kuzuluk). High-velocity and low-attenuation patterns correlate with blocks presumed to be rigid (Kocaeli, Armutlu, and Almacik blocks). The rupture traces of the largest earthquakes in this area pass generally in the transition areas between high and low velocities, while moderate and weak seismicity is mostly concentrated in low-velocity areas. Based on these results we propose and discuss the role that the Almacik block could have played in producing the largest earthquakes in the study area in the twentieth century.

Online Material: Color versions of Figures 1–15.

Introduction

This study is focused on the western part of the North Anatolian fault zone (NAFZ) (Fig. 1), which extends for more than 1500 km and contains one of the largest and most active right-lateral transform faults in the world (e.g., Barka, 1992). The tectonics of the NAFZ are controlled by the complex collision of the African, Arabian, and Eurasian plates. The high seismic activity of the NAFZ presents serious risk for people and industry in this densely populated region. During the last century, the NAFZ has ruptured over 900 km of its length and produced numerous moderate and several large ($M > 7$) earthquakes (Barka, 1996, 1999; Ambraseys and Jackson, 2000). A series of large earthquakes starting in 1939 near Erzincan in Eastern Anatolia appears to have propagated westward toward the Istanbul–Marmara region, which is located at a transition zone between the strike-slip and the extension regimes in the Aegean Sea. Within this ~100 km length zone, no significant ruptures have occurred since 1766. This area has a high potential of producing a very severe earthquake ($M > 7$) within the next few decades that would threaten the city of Istanbul (more than 13 million inhabitants) and the surrounding areas.

The western part of the NAFZ consists of a complex combination of faults and aseismic blocks. Figure 1 shows the fault segments affected by strong events in the twentieth century (Barka *et al.*, 2002). It can be seen that the Almacik block plays a particular role in producing the events of 1944, 1957, 1967, and the Düzce earthquake of 12 November 1999. The eastern part of the Kocaeli rupture (17 August 1999) corresponds to the Karadere segment, which also marks the northwest border of the Almacik block.

Previous efforts investigated the western part of the NAFZ and the Marmara Sea basin using different geological and geophysical approaches. For example, detailed investigations of the geological and tectonic structures of this area were conducted by Yilmaz *et al.* (1995), Yaltirak (2002),

*Also at Helmholtz Centre Potsdam, GFZ German Research Centre for Geosciences, Telegrafenberg, 14473, Potsdam, Germany.

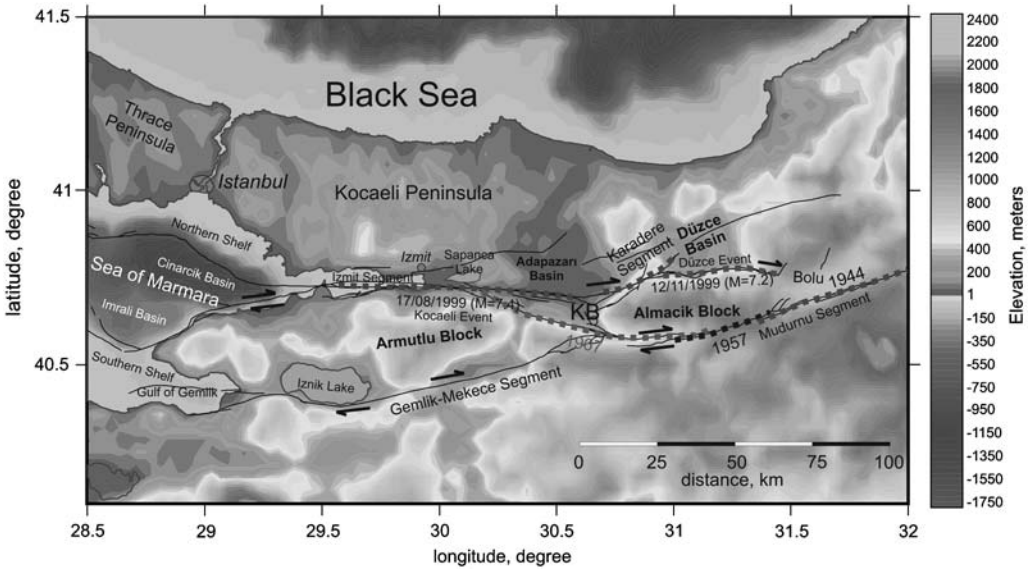

Figure 1. The main geographical units in the study area. The dotted lines depict fracture zones of the major earthquakes in the twentieth century. The information of the events (date, magnitude) is presented. KB is the Kuzuluk basin. The shapes of the faults and events are from Ambraseys and Jackson (2000), Armijo *et al.* (2002), and Yaltirak and Alpar (2002). The background is the smoothed topography/bathymetry map. Ⓔ A color version of this figure is available in the electronic edition of *BSSA*.

Armijo *et al.* (2002), and many others. Neotectonic processes along several branches of the NAFZ have been investigated by Barka (1992). Several multidisciplinary studies that consider the joint analysis of magnetic and gravity fields, electrical and magnetotelluric measurements (e.g., Honkura *et al.*, 1985; Honkura and Isikara, 1991; Honkura *et al.*, 2000) have revealed clear anomalous zones related to the variability of the extent of fracturing in different segments of the NAFZ. Similar features were identified by the analysis of the results of the combined modeling of gravity and reflection seismic data collected in the Marmara Sea region (Adatepe *et al.*, 2002). Other active source seismic investigations of the Marmara Sea and surrounding areas (Smith *et al.*, 1995; Okay *et al.*, 2000; Yaltirak and Alpar, 2002; Demirbag *et al.*, 2003; Karabulut *et al.*, 2003; Carton *et al.*, 2007) provided evidence for signatures of active faults, resulting in a detailed structure of the sedimentary cover in the pull-apart basins located in the western end of the NAFZ. The amount of relative right-lateral displacement (20–30 mm/yr) of the Anatolian block with respect to the Eurasian plate that occurs along the North Anatolian fault is based on Global Positioning System (GPS) measurements (e.g., Straub and Kahle, 1994; Oral *et al.*, 1995; Barka and Reilinger, 1997).

The crustal seismic structure in the western part of the NAFZ has been the focus of several tomographic studies performed by different research groups (e.g., Nakamura *et al.*, 2002; Aktar *et al.*, 2004; Baris *et al.*, 2005; Salah *et al.*, 2007). Most of them were based on the inversion of *P*- and *S*-wave travel-time arrivals from local seismicity recorded by stations belonging to temporary and/or permanent networks. Although these studies cover a similar area, their results often show considerable discrepancies. This seems to indicate that the obtained solutions might be unstable, affected by noise, or artifacts. It means that the information on deep structure in this area still needs to be confirmed by using other data sets and by providing convincing arguments for the robustness of the solution. For example, one of the possible reasons to explain the inconsistencies between the published models (e.g., Baris *et al.*, 2005; Salah *et al.*, 2007) might be their strong dependency on the chosen grid configurations. In fact, these studies were carried out using large node spacing that might not be suitable to image the size of the resolved anomalies. It follows that some anomalies detected in the tomographic images and represented by only one grid node might not be genuine features. It is obvious, in fact, that in this case a simple modification of the chosen grid configuration could lead to significant variations in the retrieved models. Furthermore, in some cases (e.g., Baris *et al.*, 2005) the demonstrated vertical resolution seems to be overestimated, because the velocity anomaly maps shown for different depths (0, 5, 10, and 15 km) do not show any correlation with each other. At the same time, as shown in many published studies for other regions and in the Synthetic Modeling section of this article, poorer vertical resolution with respect to the horizontal resolution is a common problem of most local earthquake tomography (LET) inversions. Therefore, we suspect that a rapid change in the velocity structure at similar depths in the mentioned studies is simply due to instabilities in the inversion. Furthermore, the indicated studies show a weak correlation between the tomographic models and the known fault system, while highly fractured media are expected to indicate large velocity changes. This also appears to be a reason for a thorough verification of these results based on independent approaches and data.

The main purpose of this study is to derive a new crustal model of the western segment of the NAFZ based on an LET scheme, using new high-quality data and paying particular attention to the reliability of the imaged lateral heterogeneities. Differently from the previous studies carried out in the area, the following was undertaken:

1. We collected a new, independent data set recorded by a permanent and a temporary network. The phase picking was carried out by one person ensuring a high level of consistency.
2. We carried out the LET inversion using the LOTOS code (Koulakov, 2009a). This code has some important features, such as quasi-continuous parameterization, which makes the resulting model grid independent.
3. We paid particular attention to the assessment of the reliability of the results. In synthetic modeling we reproduced as closely as possible the conditions of real experiments, when neither events, nor optimal 1D model were known *a priori*. Besides the synthetic modeling, we carried out an odd/even test that allowed us to assess the effect of random noise in the data. Several reconstructions adopting various starting parameters (inversion coefficients and reference models) were carried out and analyzed to check the stability of the solution.
4. Together with the results for V_P, V_S anomalies, and the V_P/V_S ratio, we present here the 3D distributions of frequency-dependent shear-wave attenuation, Q_S, derived from the inversion of the t^* data set (Bindi, Parolai, Grosser, Milkereit, and Zümbul, 2006).

Data and Algorithm

The seismological network considered in the present work is composed of 41 stations covering an area of about 220 km by 80 km along the northern branch of the North Anatolian fault, east of Istanbul (Fig. 2). The network contains 12 permanent stations installed in 1996 to monitor earthquake activity within the Sakarya and Bolu provinces (SABO network), between Sapanca Lake and the city of Düzce. The other 29 stations (19 seismometers and 10 accelerometers) were installed by the German Earthquake Task Force (GTF) for recording aftershocks of the 17 August 1999 Kocaeli M 7.4 earthquake (GTF network), either as free field or at the basement of small houses. The GTF network was continuously operating from 21 August to 22 October 1999. Unfortunately it had been removed just a few days before the Düzce event (12 November 1999, M 7.2). The average station spacing of the SABO and GTF networks was about 15 km, and the seismological equipment consisted of Mark L4-3D 1 Hz geophones, a 24 bit digitizer with a sampling rate of 100 Hz, and GPS timing. More details of the networks can be found in Baumbach *et al.* (2003).

The data set used in this study combines the information from the SABO and GTF networks. From the SABO catalog 2408 earthquakes with a corresponding 17,500 P and 4600 S picks (a minimum of 6 picks per event) that occurred between January 1998 and July 1999 and from October to November 1999 were extracted. In addition, we used 1100 aftershocks of the 1999 Kocaeli earthquake that occurred between 22 and 30 August 1999 and were recorded by both the GTF and SABO networks. About 14,000 P- and 10,000 S-handpicked arrivals were selected from those recorded by both GTF and SABO networks, excluding earthquakes with less than eight available phases. The data set also contains information about some quarry blasts (e.g., north of Adapazarı) that should be taken into account when interpreting the seismicity distribution.

For seismic tomography, we used the events with at least 12 picks available. At the stage of preliminary source location, some of the arrivals with residuals of more than 1.5 sec for P and 2 sec for S rays were rejected. Only the events located inside the network were taken into consideration. After rejecting the outliers we had 13,944 P- and 10,601 S-arrival times from 1140 earthquakes shown in Figure 2 that were used for iterative tomographic inversion and source location in the 3D velocity model.

In this study we use an updated version of the LOTOS code that is described in detail in Koulakov (2009a) and on the Web site (see the Data and Resources section). The new version of LOTOS allows for the inversion of both V_P and V_S and of V_P and the V_P/V_S ratio. Here we shortly summarize the main inversion steps.

Input data for the code only require the coordinates of the stations and the arrival times from regional and local seismicity. The hypocentral coordinates and the origin time are not strictly required because the absolute locations are determined during the execution of calculations. However, if preliminary hypocentral locations are available, they can be used to increase the speed of the calculations. In addition, a file with the starting 1D velocity model description and a set of free parameters for performing different steps (e.g., source locations, parameterization grid construction, inversion, etc.) is necessary.

The first stage of the procedure is related to preliminary source locations and the optimization of the 1D velocity model, which is performed iteratively. Each iteration consists of the following steps (see also Koulakov, 2009a):

1. Calculation of the table of reference travel times for the 1D velocity model for all possible epicentral distances and source depths.
2. Location of sources in the 1D velocity model using tabulated times that speed up the calculations. This step is based on a grid search method that makes the location very stable and allows the location of an earthquake independent of the search start point.
3. Computing the first derivative matrix that represents time variations of each ray due to unit velocity changes at different depths.
4. Simultaneous inversion for P- and S-velocity variations in the 1D model and source parameters.

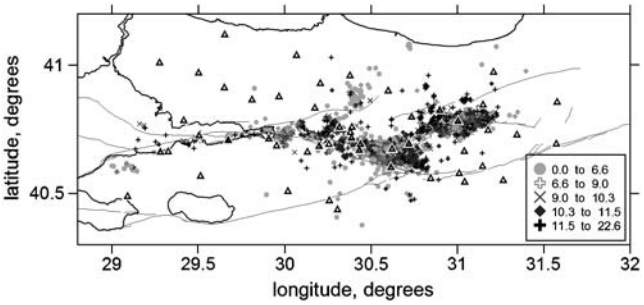

Figure 2. Distribution of stations (black triangles) and events (gray symbols) used for this study. The symbols reflect the depth of the events according to the scale. Ⓔ A color version of this figure is available in the electronic edition of *BSSA*.

The source locations and the 1D velocity model obtained after the preliminary stage are used as starting parameters for the second step of the nonlinear tomographic inversion. This part is performed in several iterations, which consist of the following steps:

1. Locating the sources using the 3D velocity model. The algorithm updates the coordinates of a source using a gradient method. The rays in a 3D velocity model are computed using the bending method.
2. Parameterization. The LOTOS code allows for the parameterization of the velocity model either with nodes or with cells. In both cases, the nodes/cells are installed according to the distribution of rays in the 1D model. The spacing of the grid is kept considerably smaller than the expected size of the anomalies in order to reduce the bias of the resulting models due to the grid configuration. Moreover, in order to further decrease the influence of the parameterization on the results, the inversion is repeated using several grids configurations with different basic orientations (e.g., 0°, 22°, 45°, and 66°). The results obtained for these grids are combined into one model by simple averaging. Examples of two grids with basic orientations of 0° and 45° are shown in Figure 3. Independence of tomographic results of grid configurations was shown in few previous studies based on the LOTOS code (e.g., Koulakov *et al.*, 2007; Koulakov, 2009a; Koulakov *et al.*, 2009).
3. The inversion was performed simultaneously for *P*- and *S*-velocity anomalies with respect to the model derived in the previous iteration and for the source parameters. Alternatively, in this study the inversion was also carried out for V_P and the V_P/V_S ratio using the algorithm described in Koulakov *et al.* (2007). The inverted velocity anomalies are damped by using two additional matrix blocks that control amplitude and smoothing of the solution. The sparse matrix is inverted using the least-squares QR method (Paige and Saunders, 1982; van der Sluis and van der Vorst, 1987).

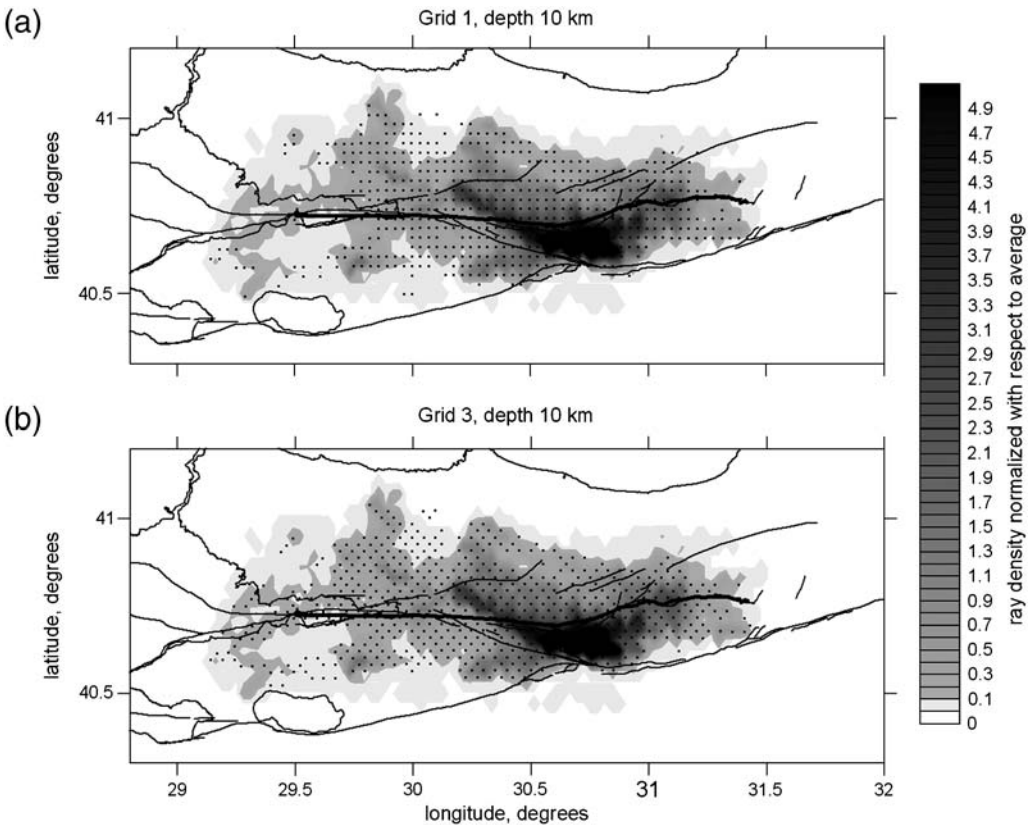

Figure 3. Density of rays in the depth interval of 7–13 km normalized with respect to the average value for the entire model. The dots indicate the distribution of nodes over the same depth interval for two different grids: (a) grid 1 with orientation 0°; (b) grid 3 with orientation 45°. Ⓔ A color version of this figure is available in the electronic edition of *BSSA*.

4. The models derived using different grids are then averaged and combined to provide a 3D model of absolute P and S velocities. This model is then used as a basic one for the next iteration that consists of the steps 1, 3, and 4.

Following Koulakov *et al.* (2007), the damping parameters were evaluated after the inversion of the synthetic data sets. The values of the free parameters were optimized by maximizing the similarity between the initial model, both in terms of amplitude and the positions of the synthetic patterns. Furthermore, performing both the inversion for $V_P - V_S$ and for $V_P - V_P/V_S$ gives additional constraints for the amplitudes of P- and S-wave velocity anomalies and reduces the uncertainty in their determination. The damping parameters in these two cases are adjusted to achieve similar amplitudes and shapes of patterns in all derived models. In particular, when performing these two inversion schemes, special attention is paid to achieving a good agreement between the S-wave velocity models that are generally the most sensitive to the kind of inversion used.

Finally, in this study we also carried out the inversion of t^* calculated from the spectra of S waves that resulted in the 3D distribution of S-wave attenuation. Innovatively, the t^*s used as input for the tomographic inversion were derived for several frequencies independently using the inversion procedure described in Bindi, Parolai, Grosser, Milkereit, and Zümbul (2006). For the first time in a local tomography, the 3D distribution of attenuation is shown for various frequencies. The response on the frequency variation provides important information about the seismic properties of rocks in the crust. The t^* data collection and results of the tomographic inversion for attenuation are presented in the section Attenuation Tomography.

Observed Data Inversion

As described in the previous section, the observed data processing starts with preliminary source locations and optimization of the 1D velocity model. In order to estimate the stability of the solution, calculations using different starting models are carried out. Figure 4 shows the results of the optimization procedure starting from four different models. The starting models (thin dashed lines) differ significantly for gradient and absolute values of velocities as well as for the assumed V_P/V_S ratio. The resulting 1D V_P and V_S profiles converge to similar values for the depth interval 5–15 km. At the same time, velocities are not well constrained above 5 km and below 15 km depth. Model 4, which provided the minimum root mean square (rms) of the residuals, was adopted for starting the 3D tomographic inversion. Having a low-velocity uppermost layer, it may better resemble the crustal structure in the area where thick sedimentary basins exist.

The rms values of the P and S residuals and their reductions after five iterations according to the $V_P - V_S$ scheme

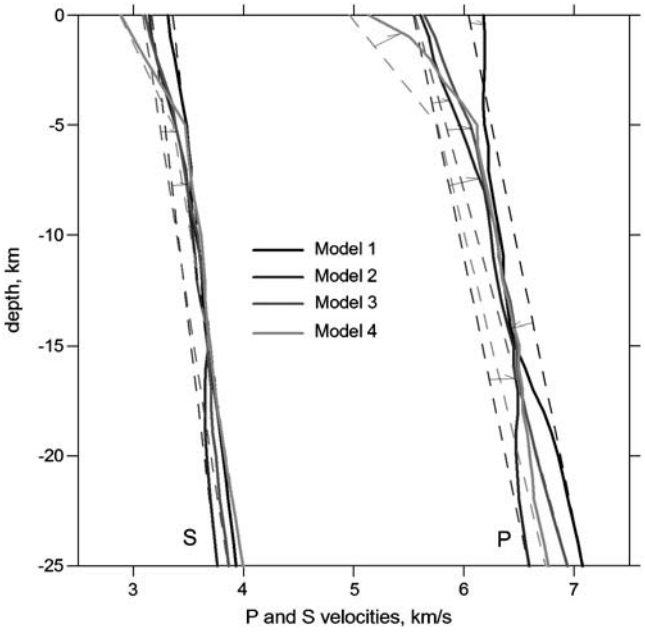

Figure 4. Results of optimization for the 1D velocity model with the use of four different starting models indicated with different gray shades (thin dashed lines show the starting 1D models; bold lines are optimization results). Arrows mark the velocity change due to optimization. Ⓔ A color version of this figure is available in the electronic edition of *BSSA*.

are shown in Table 1. The residuals of the first iteration correspond to the location in the 1D model. Values corresponding to the following iterations show how the 3D velocity inversion leads to an improved data fit. It is worth noting that the values of the residuals of the used data set appear to be already quite low initially (0.137 and 0.255 sec for P and S data, respectively) when compared to those for data sets collected in other areas. For example, for the case of a central Java data set (Koulakov *et al.*, 2007) in the first iteration, the rms of P and S residuals were 0.388 and 0.623 sec. For the Toba caldera (N. Sumatra) data set (Koulakov *et al.*, 2009) slightly smaller values, 0.280 and 0.433 sec, were found for P and S waves, respectively. Note that the same algorithm was used for data processing in the present and in the previously mentioned studies. The rms of the initial residuals can be used as an *a priori* indicator of the amplitude of the velocity anomalies. Thus, in the NAFZ area, velocity

Table 1

rms Values of the P- and S-Wave Residuals and the Variance Reductions after Five Iterations for the $V_P - V_S$ Inversion Scheme

Iteration	rms dtp* (sec)	rms dts* (sec)	Reduction P (%)	Reduction S (%)
1	0.1370	0.2551	0	0
2	0.1031	0.1664	24.29	33.22
3	0.0920	0.1526	32.41	38.77
4	0.0863	0.1474	36.58	40.85
5	0.0834	0.1445	38.75	41.99

*rms dtp and rms dts stand for the P- and S-wave residuals, respectively.

contrasts appear to be 2–3 times smaller than in the previously mentioned subduction zones. The small values of residuals after the final fifth iteration confirm the high quality of the phase picking in this study.

For the $V_P - V_P/V_S$ scheme, the variance reduction shown in Table 2 is much weaker. However, this fact does not mean that the models obtained in the later case are worse. The main reason for such differences might be related to the fact that in the case of inverting for V_P/V_S we minimize the differential $P - S$ residuals, while in the $V_P - V_S$ scheme, the P and S residuals are minimized separately. The statistics presented in Tables 1 and 2 do not account for values of differential residuals.

The resulting P- and S-velocity anomalies with respect to the 1D starting model 4 (Fig. 4) derived by $V_P - V_P/V_S$ inversion are shown in Figure 5 in four horizontal slices at 5, 10, 15, and 25 km depth. The corresponding results for the V_P/V_S ratio are depicted in Figure 6. Note that due to the used inversion scheme, the V_S anomalies are derived indirectly by the division of V_P/V_S into V_P. An inversion for V_P and V_S was carried out, and the free parameters for inversion (smoothing and amplitude damping) were adjusted to obtain similar shapes and amplitudes of anomalies with respect to the previous inversion. The comparison of S-wave velocity anomalies at a depth of 5 km obtained for the cases of $V_P - V_P/V_S$ and $V_P - V_S$ inversions (Fig. 7) shows that the shape of the main patterns and their amplitudes are quite similar. In fact, consistency of the results in these two cases is not obvious. Having free parameters (e.g., damping and smoothing) results in amplitudes of the inverted fields to be computed with some degree of uncertainty. Dividing or multiplying these values in turn increases the overall uncertainty. Thus, V_P/V_S computed from dividing V_P by V_S in the $V_P - V_S$ scheme is not automatically the same as the V_P/V_S ratio derived from the $V_P - V_P/V_S$ inversion scheme. Similarly, S-wave anomalies may appear significantly different in these two schemes if the damping parameters are not correct. Performing both schemes gives us a possibility to reduce the ambiguity in defining the damping coefficients.

Repeating the inversion using two independent subsets of data (e.g., odd and even number of events in the catalog) allows an assessment of the bias in the tomographic images due to random noise in the data. If the noise plays an important role in the data, it will lead to different inversion results.

Table 2

rms Values of P- and S-Wave Residuals and the Variance Reductions after Five Iterations for the $V_P - V_P/V_S$ Inversion Scheme

Iteration	rms dtp* (sec)	rms dts* (sec)	Reduction P (%)	Reduction S (%)
1	0.1370	0.2551	0	0
2	0.1155	0.2458	15.68	3.63
3	0.1070	0.2219	21.91	13.01
4	0.1044	0.2042	23.83	19.92
5	0.1033	0.1920	24.59	24.70

*rms dtp and rms dts stand for the P- and S-wave residuals, respectively.

The results obtained by such a test are shown in Figure 8. Note that the calculations were carried out according to the same scheme and using the same free parameters as used for inverting the entire data set shown in Figures 5 and 6. Results show practically identical patterns in V_P, V_S, and V_P/V_S, independent of the subset of data used, therefore suggesting a fairly high quality of phase picking and a low-noise level. This is confirmed by the low values of the final residuals shown in Table 1.

Synthetic Modeling

Synthetic modeling is an important stage that is aimed at assessing the spatial resolution provided by the data and algorithm. Furthermore, synthetic tests allow the evaluation of the optimal values of the free parameters (e.g., amplitude damping and smoothing) that can in turn be used for the inversion of the observed data set. The generation of the synthetic data set and its inversion should be carried out while trying to reproduce as much as possible the conditions faced during the inversion of the observed data. Following Koulakov (2009a), the synthetic tests have been carried out according to the rules that follow:

1. After computing the synthetic travel times in a synthetic model, the coordinates and origin times of the sources are forgotten. This step can be done by randomly biasing the sources from their true locations, or locating them at any point within the study area.
2. The true 1D model should also be forgotten. The processing of the synthetic times should start from an *a priori* wrong model that is optimized based on the same algorithm as used in the real case.
3. Random noise is added to the travel times, and its rms is defined according to the values of the residuals after the observed data inversion.
4. All the calculation steps and all the free parameters are identical to the case of the observed data processing.

First of all, we have performed several traditional checkerboard tests. In the first test, we explored the horizontal resolution. In this case, the synthetic anomalies are defined as periodic alternated positive and negative anomalies of 20 km lateral size that remain unchanged at all depths (Fig. 9). We used many different checkerboard tests with 10, 15, 20, 30, and 40 km size. A 20 km checkerboard seems to be the most representative as it has the same order of size as the pattern retrieved from the measured data inversion. The amplitudes of anomalies were ±4% and ±7% for P- and S-wave models, respectively. These anomalies produced variations in the V_P/V_S ratio ranging from 1.69 to 1.79. The anomalies are defined with respect to the true 1D velocity distribution, which remains unknown when performing the inversion. The true synthetic 1D model and the starting one in this case were likely to be different; hence, the reconstruction started with optimizing the 1D model. The synthetic times were computed by the bending ray tracing

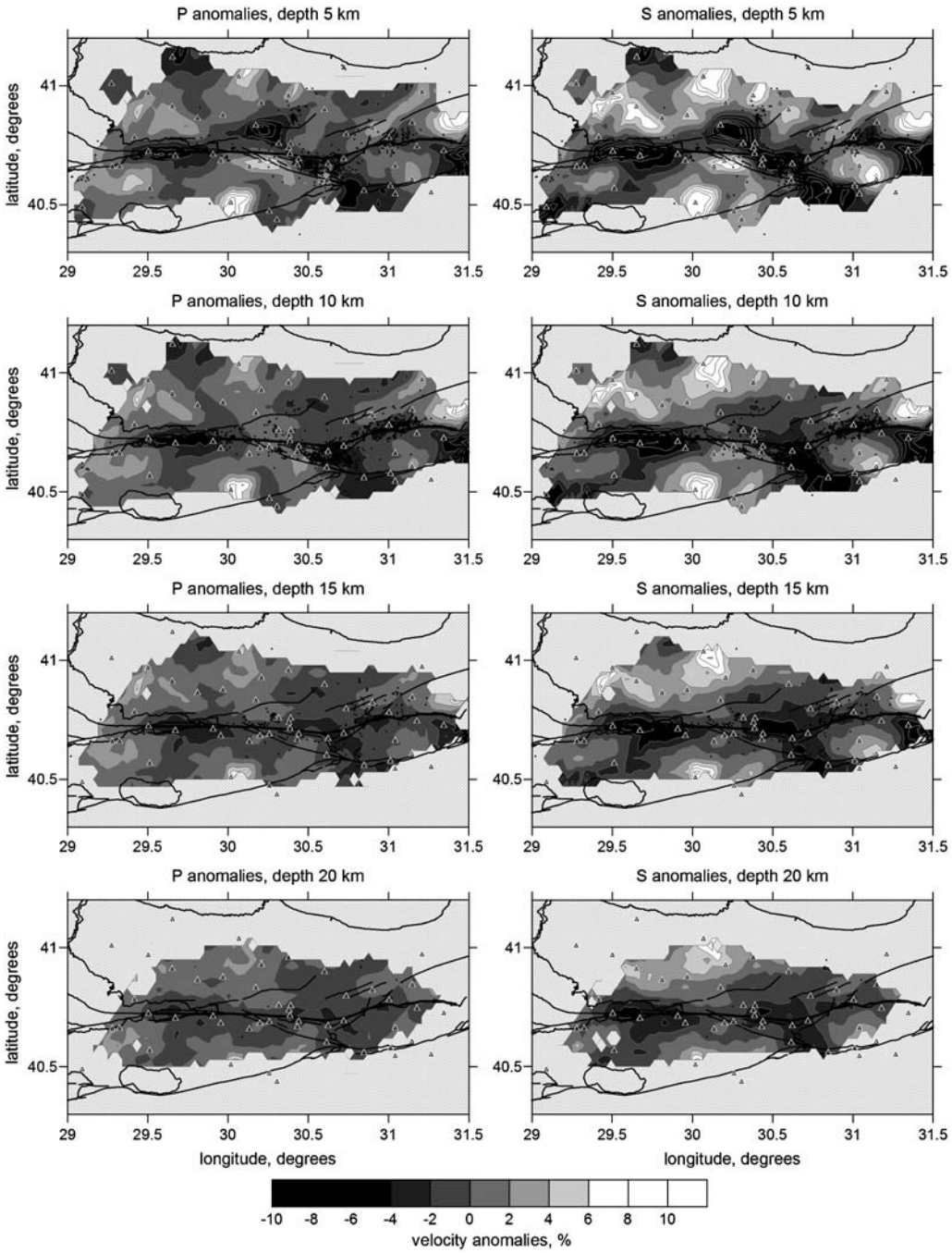

Figure 5. Resulting *P*- and *S*-velocity anomalies after inversion according to the $V_P - V_P/V_S$ scheme. The velocity anomalies are given with respect to the optimized 1D model. The lines show the coast and main faults, the same as in Figure 1. The black dots indicate events around the corresponding depth level. The triangles indicate stations used in this study. Ⓔ A color version of this figure is available in the electronic edition of *BSSA*.

algorithm and then perturbed by random noise with an rms of 0.06 and 0.1 sec for *P*- and *S*-wave data, respectively. All the steps were done according to the $V_P - V_P/V_S$ inversion scheme, and all the free parameters were the same as those used for computing the main results presented in Figures 5 and 6. The reconstruction results for the depths of 5 and 15 km are shown in Figure 9. This test reveals limitations in the horizontal spatial resolution. In fact, despite the rather large number of data and their high quality, the distribution of rays appears to be not the most suitable for tomographic inversions. Most events are located in the central part of the study area inside the network. While this is good for the accurate location of the sources, the absence of out-of-network events drastically limits the spatial resolution of

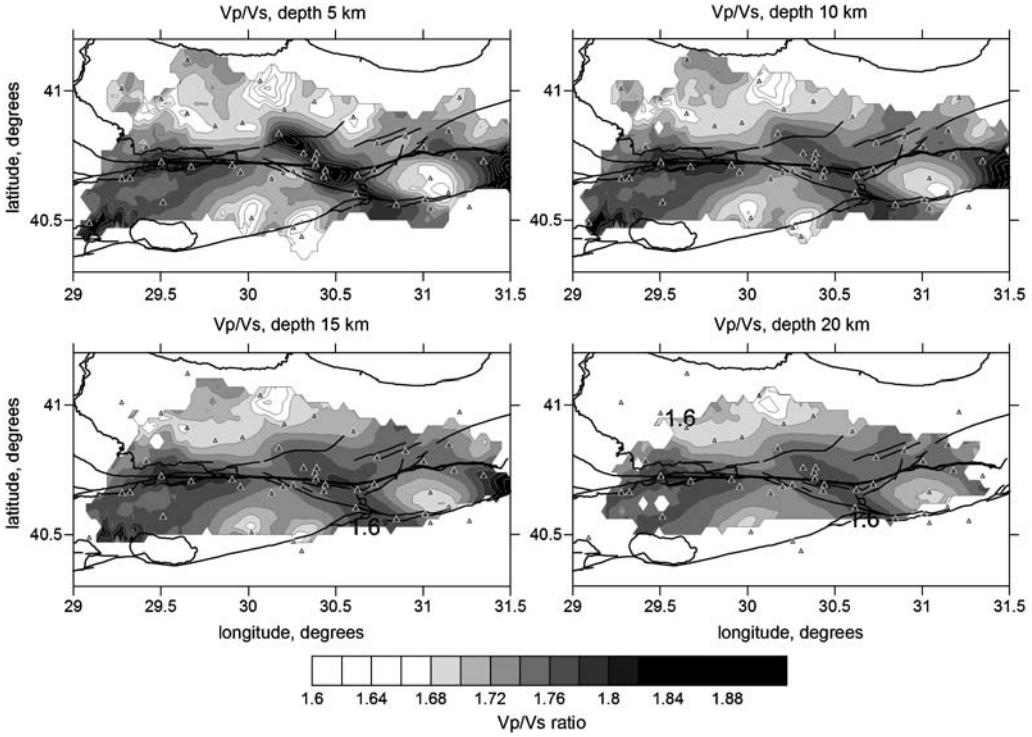

Figure 6. Resulting absolute values of the V_P/V_S ratio after inversion according to the $V_P - V_P/V_S$ scheme. The lines show the coast and main faults, the same as in Figure 1. Triangles indicate stations used in this study. Ⓔ A color version of this figure is available in the electronic edition of *BSSA*.

the tomographic images (Koulakov, 2009b). As a result of such an unfavorable configuration of the observation system, the satisfactory reconstruction is only observed nearby the fault area, while outside the NAFZ we observe considerable diagonal smearing of anomalies.

A poorer resolution is observed in the vertical sections. The input model used to assess it has velocity anomalies alternating in the east–west direction (Fig. 10a) while the velocity remains constant in the south–north direction (for the same depth range). The positive and negative anomalies are alternated in the vertical direction at depths of 7, 27, 47 km, etc. The reconstructed anomalies are shown in Figure 10 along three vertical (Fig. 10b–d) and two horizontal cross sections (Fig. 10e,f). The results show that only in one cross section (Fig. 10c, which passes through the fault area) the inversion is able to reconstruct the interface at 7 km depth. In all the other sections this feature is not detectable. This is better highlighted in the horizontal section at 15 km depth where different polarity anomalies are only observed in the central part of the study area where most of events are located. This test shows that any vertical velocity variations observed in the results of the inversion should be treated with care because of poor vertical resolution.

Figure 11 shows the results of a further synthetic test aimed at reconstructing the *P*- and *S*-wave velocity structure derived by the inversion of observed data. Shapes and amplitudes of synthetic patterns (left-hand column in Fig. 11) were obtained after thorough tuning while performing

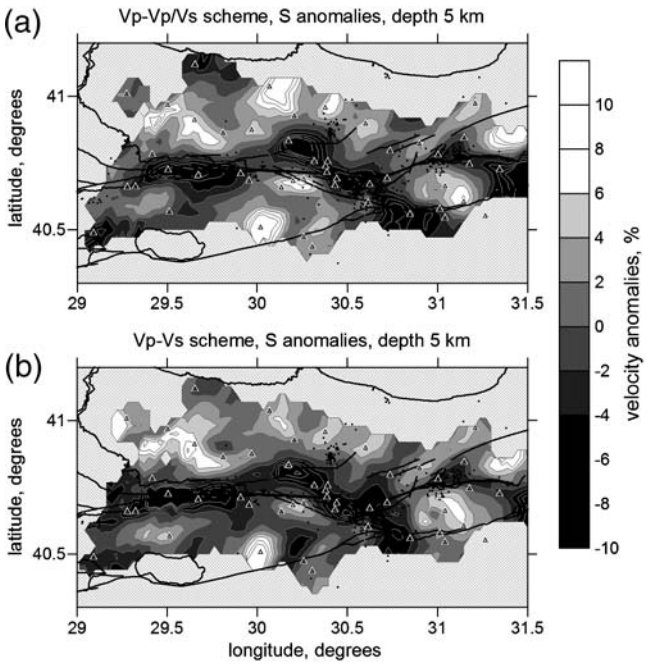

Figure 7. *S*-wave velocity anomalies at 5 km depth derived from inversions according to two different schemes: (a) for V_P and the V_P/V_S ratio; (b) for V_P and V_S. Ⓔ A color version of this figure is available in the electronic edition of *BSSA*.

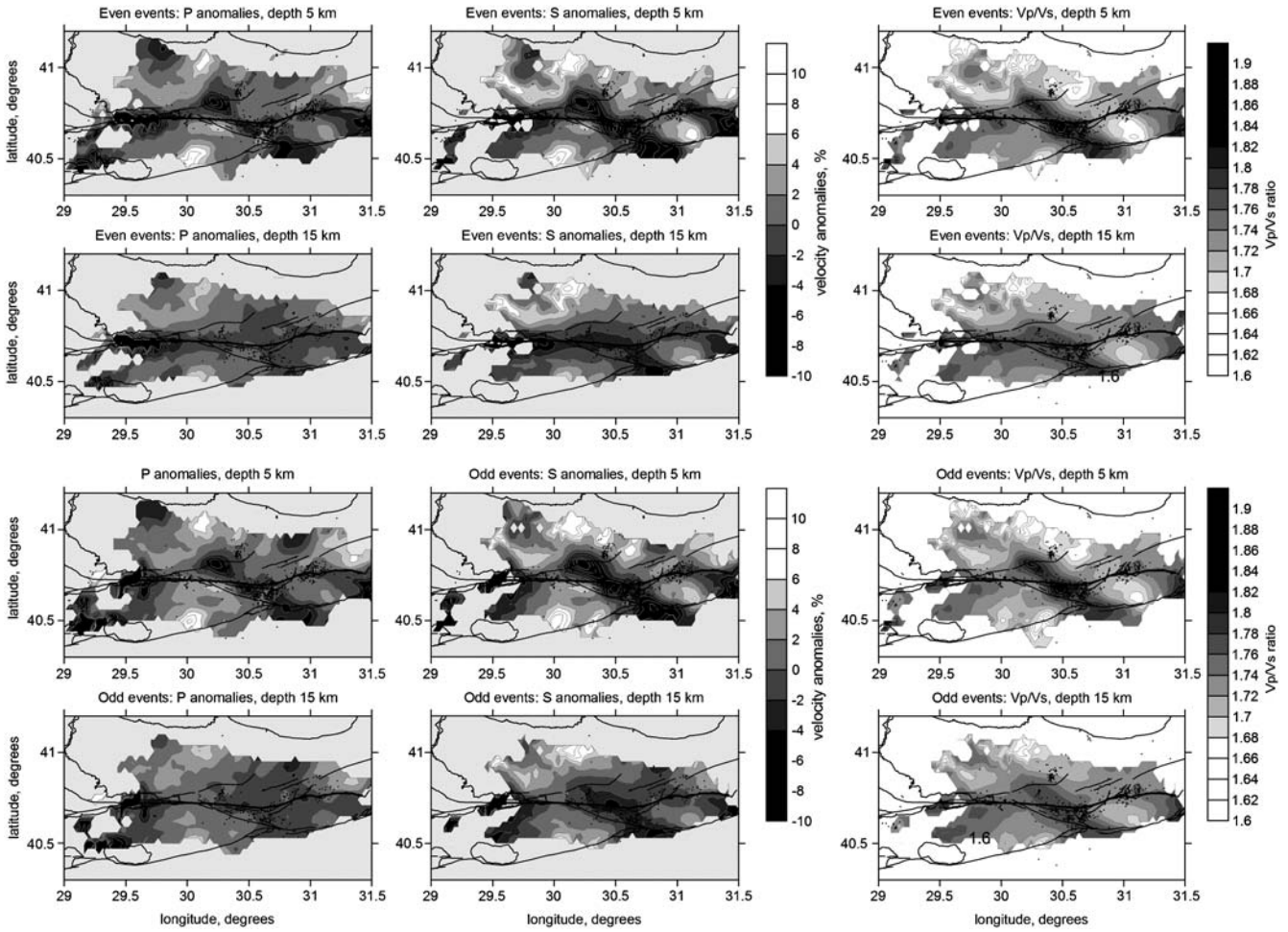

Figure 8. Results of the inversion according to the $V_P - V_P/V_S$ scheme for two independent data subsets with even (upper two rows) and odd (lower two rows) events. The *P*- and *S*-wave anomalies and the V_P/V_S ratios are shown at 5 and 15 km depth. Ⓔ A color version of this figure is available in the electronic edition of *BSSA*.

several trials of the full forward and inverse modeling procedure. After computing the synthetic travel times using the bending algorithm of 3D raytracing, the travel times were perturbed with noise of 0.09 and 0.14 sec rms for *P*- and *S*-wave data, respectively, which provide the same variance reduction as in the real case. The inversion was performed according to the procedure used for computing the main results presented in Figures 5 and 6, that is, using the $V_P - V_P/V_S$ inversion scheme. This test provides realistic estimates for the amplitudes of anomalies in the input model, although it highlights that the resulting *S*-wave velocity model provides overestimated amplitudes with respect to the input one. The same overestimation can be expected in the case of the observed data. Because the reconstruction results in Figure 11 are similar to those in Figures 5 and 6, we believe that the magnitude of the anomalies imposed in the synthetic model (left-hand column in Fig. 11) is representative of those existing in the real Earth. In particular, based on this test the velocity decrease inside the fault area with respect to the outside regions can be estimated to be about 7% for *P*-wave velocities and 12% for *S*-wave velocities.

Attenuation Tomography

The attenuation along the path between source and receiver can be estimated from the amplitude spectra of body waves. For each considered frequency f, the Fourier spectra $F_{ij}(f)$ of earthquake i recorded at station j can be expressed as (e.g., Andrews, 1986)

$$F_{ij}(f) = S_i(f)A_{ij}(f)Z_j(f), \tag{1}$$

where S_i represents the contribution of source i, A_{ij} represents the attenuation of the seismic waves along the path, and Z_j describes the site effects at station j, including the instrument response. The attenuation along the path can be parameterized as follows:

$$A_{ij}(f) = G(r_{ij}) \exp\left(-\frac{\pi f t_{ij}}{Q_{ij}}\right), \tag{2}$$

where $G(r_{ij})$ is the geometrical spreading, r_{ij} is the hypocentral distance, t_{ij} is the travel time, and Q_{ij} is the apparent

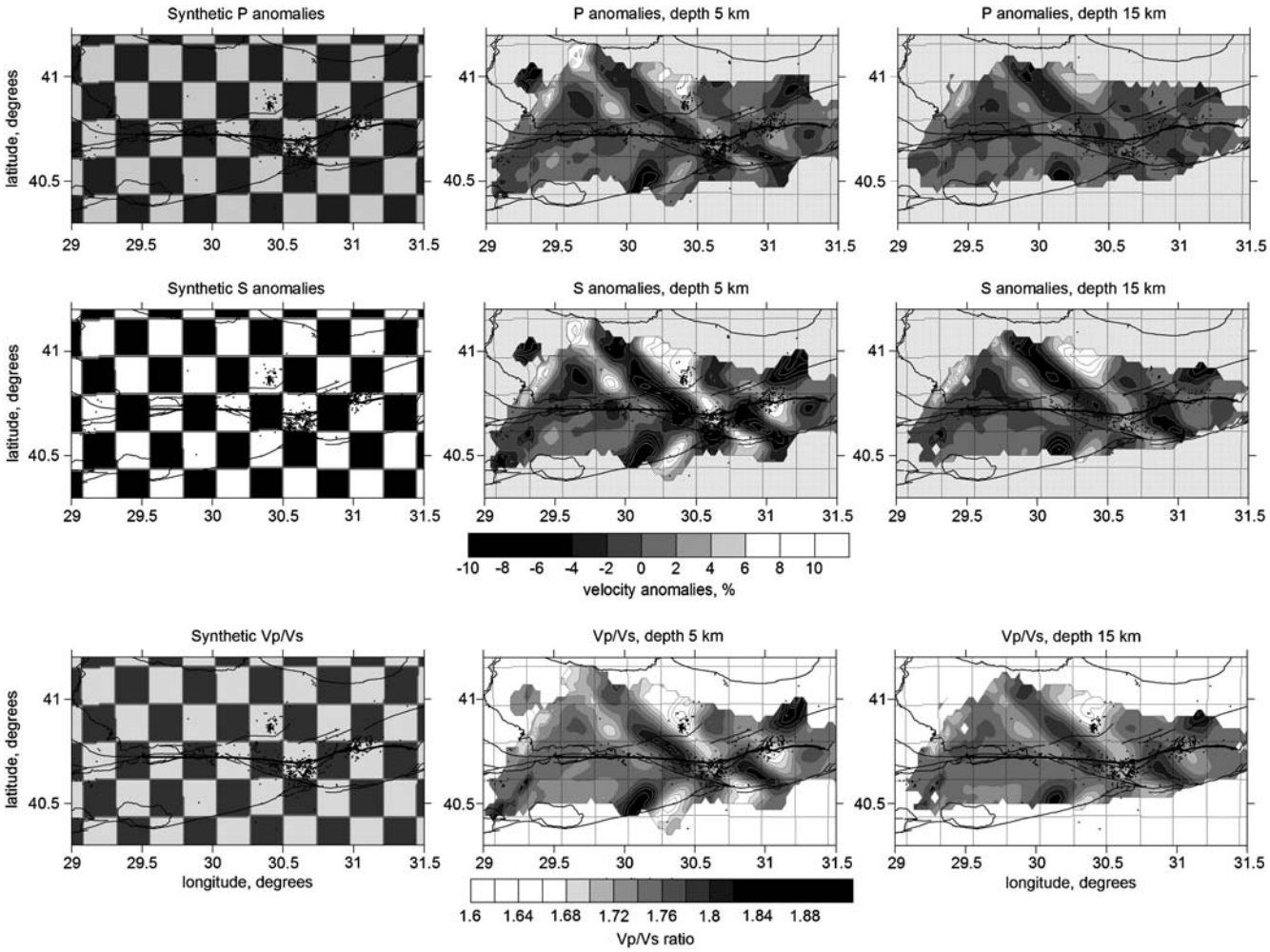

Figure 9. Results of the checkerboard test with reconstruction according to the $V_P - V_P/V_S$ scheme. The synthetic V_P and V_S anomalies and the V_P/V_S ratio are shown in the left-hand column. The reconstruction results after five iterations at the depths of 5 and 15 km are shown in central and right-hand columns. The shape of the synthetic model is indicated with thin lines. Ⓔ A color version of this figure is available in the electronic edition of *BSSA*.

quality factor along the path. The cumulative attenuation along the path ij can be described by introducing the t^* operator (Kanamori, 1967; among others):

$$t^*_{ij} = \int_{\text{path}_{ij}} \frac{dr}{Q(r)v(r)}, \tag{3}$$

where $v(r)$ is the seismic velocity. Then, equation (1) can be rewritten as

$$F_{ij}(f) = S_i(f)G(r_{ij})\exp(-\pi f t^*_{ij})Z_j(f). \tag{4}$$

In this work, we use equation (4) to compute the t^* parameter for shear waves considering the source and site spectra previously derived by Parolai *et al.* (2007). They inverted a set of 3871 waveforms recorded by the stations of the SABO and GTF networks by applying a nonparametric generalized inversion technique (e.g., Castro *et al.*, 1990). By correcting the Fourier amplitude spectrum $F_{ij}(f)$ for the source and site terms, from equation (4) we obtain

$$t^*_{ij}(f) = -\frac{1}{\pi f}\ln\left[\frac{r_{ij}F_{ij}(f)}{S_i(f)Z_j(f)}\right], \tag{5}$$

where the $1/r$ decay has been assumed for geometrical spreading $G(r)$. Details about the followed procedure can be found in Bindi, Parolai, Grosser, Milkereit, and Zümbul (2006). It is worth noting that the t^* values estimated from equation (5) are frequency dependent. Generally the frequency dependence of the apparent quality factor (and in this case of the t^*) is attributed to the scattering contribution to the attenuation. However, in this study area, Bindi, Parolai, Grosser, Milkereit, and Karakisa (2006) showed that as strong frequency dependence was also shown by the intrinsic quality factor. Therefore, the choice of considering the frequency dependence of Q seems to be appropriate. Figure 12 shows the t^* versus distance for 4 and 12 Hz. On average, t^* increases with distance, assuming, for the longest distances, values around 0.25 and 0.15 sec for 4 and 12 Hz, respectively. For distances shorter than 40 km, the considered paths

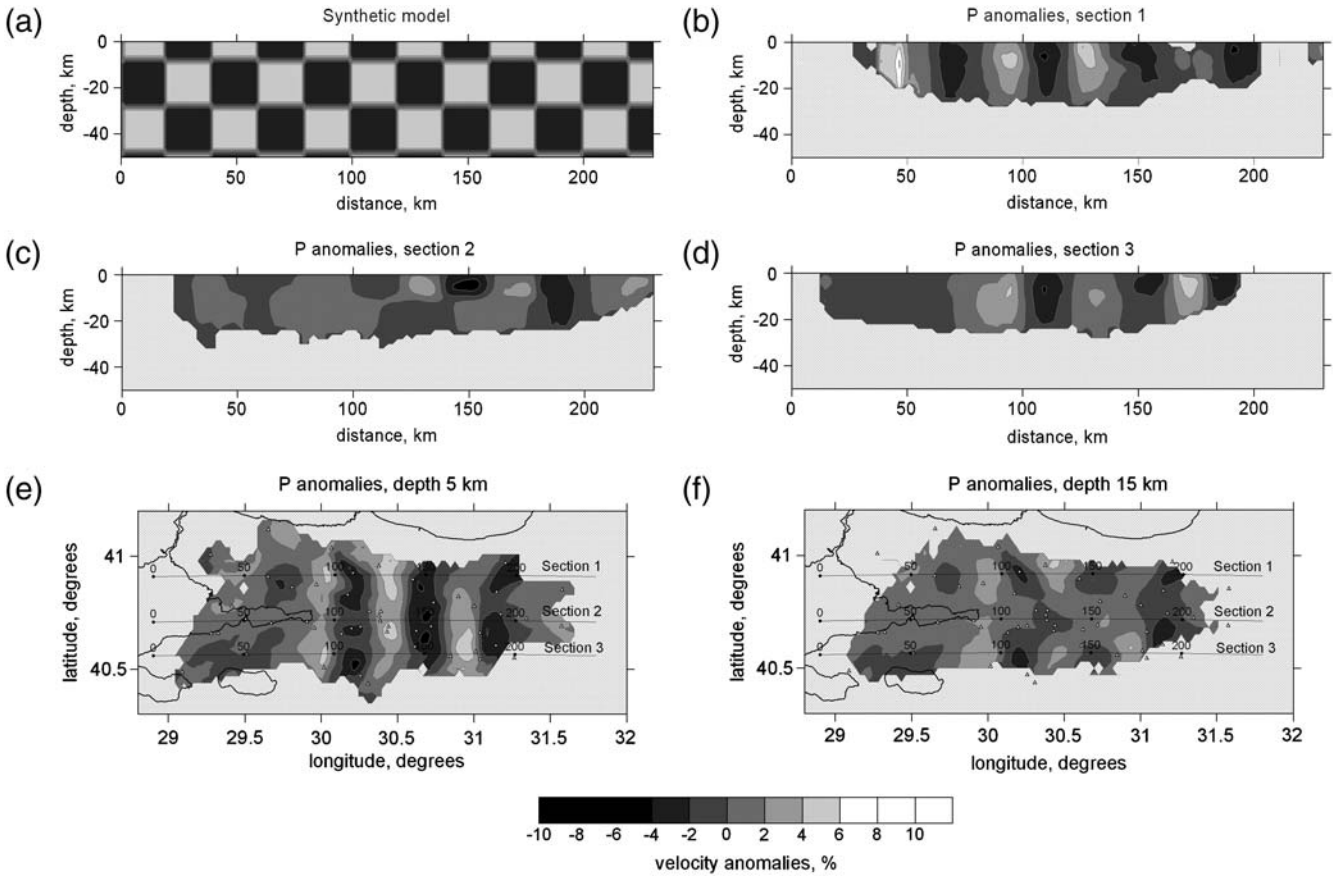

Figure 10. Synthetic test that shows poor vertical resolution provided by the existing data set. (a) Synthetic anomaly in vertical sections (same for all); (b–d) reconstruction results in the Introduction, the Data and Algorithm section, and the Observed Data Inversion section. (e and f) Map view of the reconstructed anomalies at depths of 5 and 15 km. Ⓔ A color version of this figure is available in the electronic edition of *BSSA*.

sample well the entire azimuth range, while for larger distances, the azimuths are mainly distributed in the azimuth range 70°–130°. In particular, paths longer than 140 km cross the investigated area along the east–west direction, that is, parallel to the North Anatolian fault.

The computed t^* values can be inverted through equation (3) to map the 3D variation of the quality factor Q. It is important that values of t^* were obtained for different frequencies that give us a chance to explore the frequency dependence of shear-wave attenuation.

The attenuation tomography is much easier to implement compared to the travel-time LET scheme described in previous sections. Here we use an algorithm that was previously applied for the investigation of central Chile (Koulakov *et al.*, 2006). It presumes one step linear inversion and that sources remain fixed. The rays and locations of events are taken from the final iteration of travel-time inversion corresponding to the S model presented in Figure 5. The parameterization algorithm with rotated adaptive grids is the same as used for velocity tomography.

In Figures 13 and 14 we present the inversion results for the depth levels at 5, 10, 15, and 20 km, which correspond to two different frequencies: 2.09 and 12.59 Hz, respectively. Note that the resulting attenuation, $1/Q_S$, decreases with increasing the frequency: the scale in the first case ranges up to 40×10^3, while for the second case it is up to 12×10^3. The resulting attenuation at the depth of 10 km computed for eight different frequencies ranging from 21.14 to 0.58 Hz are shown in Figure 15.

For all frequencies, the strongest attenuation is observed in the uppermost level at 5 km depth. However, the details of the uppermost structure appear to be different for different frequencies. For the frequency of 12.59 Hz (Fig. 14), we observe a patch of high attenuation reaching 13×10^3, which coincides with the Adapazarı basin (see Fig. 1). It means that at this relatively high frequency the seismic attenuation is most sensitive to the distribution of sediments. This is consistent with the results of Bindi, Parolai, Grosser, Milkereit, and Zümbul (2006). For the frequency of 2.09 Hz (Fig. 13), this basin is not clearly seen in the uppermost section. The higher attenuation patterns in this case correspond to the areas of large relief contrasts (e.g., in the eastern part of the Armutlu block and northwest to the Karadere segment).

For the deeper parts, the resulting patterns remain unchanged in shape for all frequencies (see, e.g., the results for the eight different frequencies for the depth of 10 km).

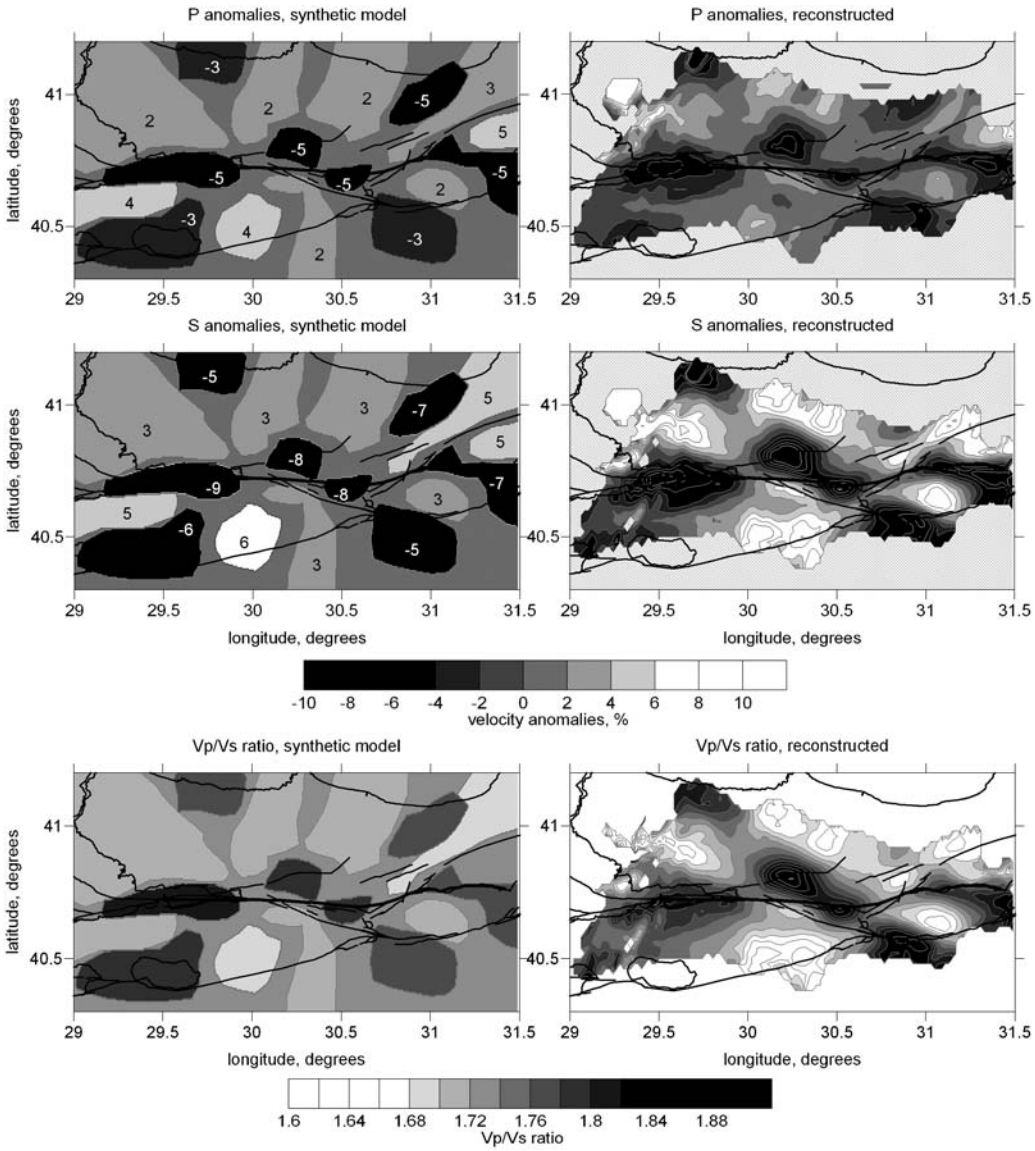

Figure 11. Reconstruction of a synthetic model with realistic distribution of patterns. The left-hand column is the configuration of P, S anomalies, and the V_P/V_S ratio in the synthetic model. The numbers depict amplitudes of anomalies in percent. The right-hand column presents the reconstruction results for the corresponding values at the depth of 5 km. These results are computed based on the $V_P - V_P/V_S$ inversion scheme with the same free parameters as used to obtain the main results in Figures 5 and 6. Ⓔ A color version of this figure is available in the electronic edition of *BSSA*.

Relatively high attenuation is observed in the Sapanca segment of the fault, where the Kocaeli event occurred. To the south and to the north of this fault segment, we observe two areas of lower attenuation (higher goodness), which correspond to the rigid part of the Kocaeli and Armutlu blocks.

It is rather unexpected to observe the low-attenuation area to the east of 30.1° longitude. This pattern covers the area with a high concentration of weak and moderate events, and it is clearly expressed by low velocities and high V_P/V_S ratios in our tomographic results. All these facts provide evidence that this is an area of high rate of fracturing, and it would be more natural to observe higher attenuation there.

Discussion and Conclusions

The resulting distributions of seismic parameters show clear correlation with the known tectonic features in the study area, which is an indirect argument for the reliability of the obtained models. At shallower depths (5 km), although some smearing of the anomalies in the northwest–southeast direction exists, as evident by the synthetic test, low velocities both for P and S waves with large V_P/V_S ratio are mainly observed either close to the main segments of the NAFZ (in Gölcük, Sapanca, and Karadere) or in proximity of the alluvial basins (of Izmit, Adapazarı, and Düzce). These results are also consistent with the findings of Baumbach *et al.* (2003). While the large V_P/V_S ratio in the alluvial

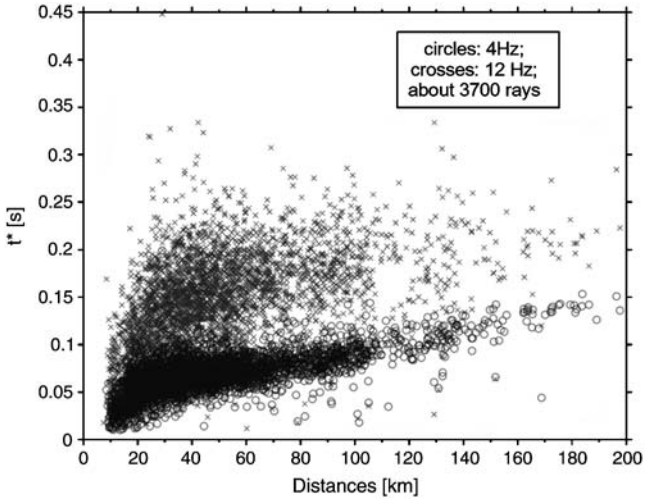

Figure 12. Variation of t^* versus distance for two indicative frequencies: circles, 4 Hz; crosses, 12 Hz. Ⓔ A color version of this figure is available in the electronic edition of *BSSA*.

basin, as well as the low-quality factor, agree with the presence of low velocity and saturated sedimentary cover, the same values associated with the main faults might imply fracturation and fluid penetration in the fault zone. On the other hand, the main unfractured parts of the crust such as the Kocaeli, Armutlu, and Almacik blocks are clearly expressed as high-velocity structures.

Figure 16a shows our qualitative reconstruction of the locations of the main blocks in the study area corresponding to the time of about 2 m.y.a. It is based on the assumption of a displacement rate of ~2 cm/yr (e.g., Barka and Reilinger, 1997) that roughly corresponds to a 40 km displacement. In this case, the Adapazarı basin was just in front of the Izmit Bay of the Marmara Sea. Looking at the distribution of low-velocity anomalies, we see that a large low-velocity pattern that is observed beneath the Adapazarı basin might be a whole unit with a low-velocity pattern in the Armutlu block south to the Izmit Bay. It may represent a block with other physical properties (e.g., composition) that are expressed by low velocities. According to this interpretation, this block was broken in two parts about 2 m.y.a. The Adapazarı basin is expressed by relatively low seismicity (the cluster of events in the northeast boundary of this block correspond to industrial quarry blasts and is not related to natural seismicity). This fact, as well as the low attenuation (green contour line in Fig. 16b) observed in the Adapazarı basin, probably indicates that this block remains unfractured nowadays.

This interpretation reveals a special role of the Almacik block in the tectonic evolution of the fault zone. Located between the Eurasian and Anatolian plates, which move in opposite directions, this block was partly driven by each of them. It may appear that such displacement locks in turn the faults on the northern and southern boundaries of the Almacik block. It may cause an accumulation of considerable elastic energy that is released during catastrophic earthquakes. This kinematic behavior is in good agreement with the apparent role of the Almacik block in producing large earthquakes. In the twentieth century, at least five large

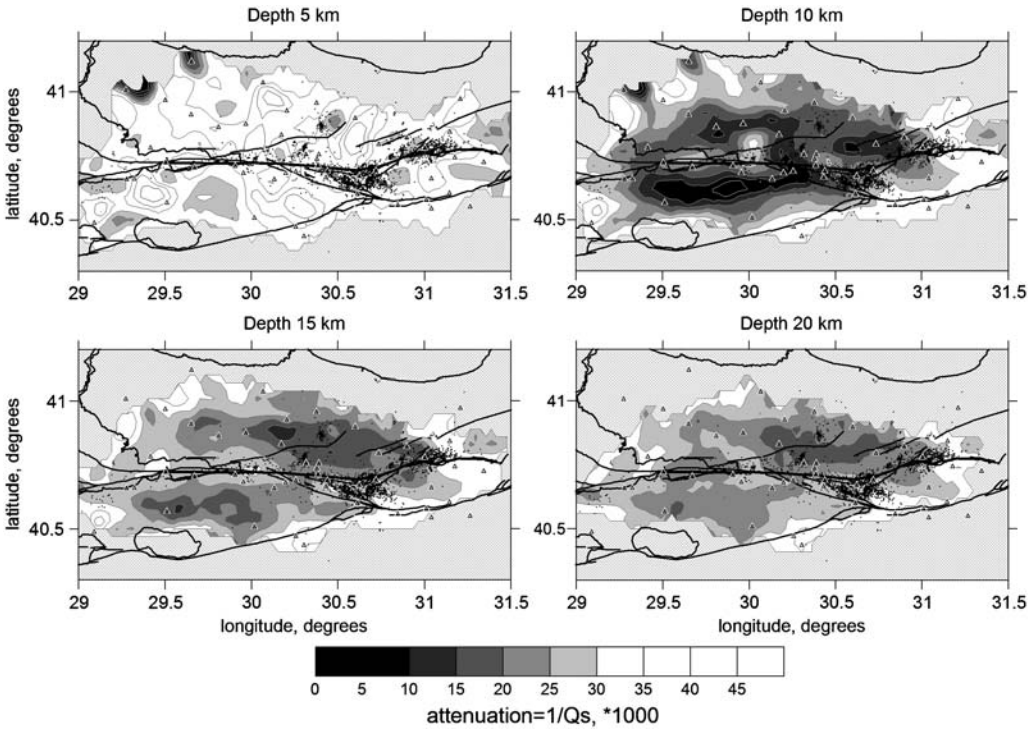

Figure 13. Distribution of *S*-wave attenuation, $1/Q_S$, in four horizontal sections for the frequency of 2.09 Hz. The dots indicate events used for inversion; triangles depict seismic stations. Ⓔ A color version of this figure is available in the electronic edition of *BSSA*.

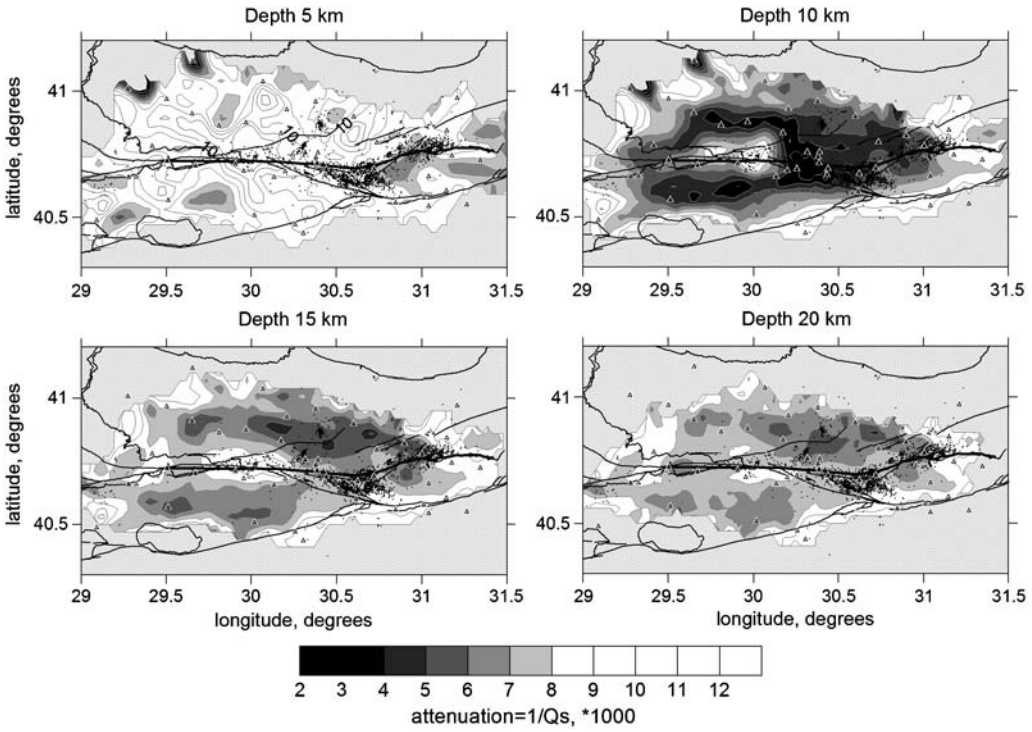

Figure 14. Same as Figure 13 but for a frequency of 12.59 Hz. Ⓔ A color version of this figure is available in the electronic edition of *BSSA*.

earthquakes (1944, 1957, 1967, 12 November 1999, and part of the 17 August 1999 event) occurred along its southern and northern boundaries (see Fig. 1).

It is also important that the strong earthquakes often occur along the faults that pass in the transition zone from high- to low-velocity patterns. On the other hand, weak and moderate seismicity is mostly concentrated in low-velocity zones. This observation can be explained by the assumption that low-velocity patterns in the crust often represent highly fractured soft rocks that cannot accumulate strong elastic energy. These moderate and weak stresses are released with relatively weak and numerous seismicity. On the contrary, the blue high-velocity areas usually represent rigid blocks. If these blocks are located close to a highly fractured soft fault zone, it is difficult to accumulate sufficient energy to rupture them; hence, strong events probably will not occur there either. The highest potential for the accumulation of strong energy and its release in catastrophic events is in the transition areas between higher and lower velocities.

These findings are in general agreement with Bouchon and Karabulut (2008), who investigated aftershock signatures of large earthquakes by a supershear mechanism that assumes the rupture occurs at speeds exceeding the shear-wave velocity of rocks. For three different supershear earthquakes, they found that the planes of the main ruptures are remarkably quiet and most of aftershocks are concentrated outside the major fault. They explain the activation of off-fault structures by the shock wave radiation, which produces high stresses around the fault. For the Düzce and Izmit earthquakes of 1999, the supershear mechanism was proposed in earlier studies (e.g., Tibi *et al.*, 2001). In our tomograms, most of the moderate and weak earthquakes occur in low-velocity segments that are located outside the main rupture planes and might be related to highly fractured rock volumes.

The curvature of the northern boundary of the Anatolian plate, which moves westward, causes an opening of a pocket near the western edge of the Almacik block, corresponding to the Kuzuluk basin (indicated with KB in Fig. 16b). This process results in the opening of a pull-apart zone, which is clearly expressed by the dense distribution of weak and moderate seismicity and low-seismic velocities in our tomograms. The west–east extension in the Kuzuluk basin is also corroborated by the recent focal mechanism calculations by Tibi *et al.* (2001). Many thermal sources (e.g., Greber, 1994; Belin *et al.*, 2002) that play an important role in the tourist industry of the Kuzuluk district may also support the concept of an active pull-apart extension. A similar mechanism of the pull-apart basin opening was earlier proposed for the Marmara Sea (e.g., Armijo *et al.*, 1999; Pondard *et al.*, 2007).

The frequency-dependent tomographic images show smaller Q_S values in the shallow crustal layer with the lower values in the area affected by major faulting or where the thick sedimentary basins are located. This result is in agreement with those of Bindi, Parolai, Grosser, Milkereit, and Zümbul (2006) who found similar evidence from a

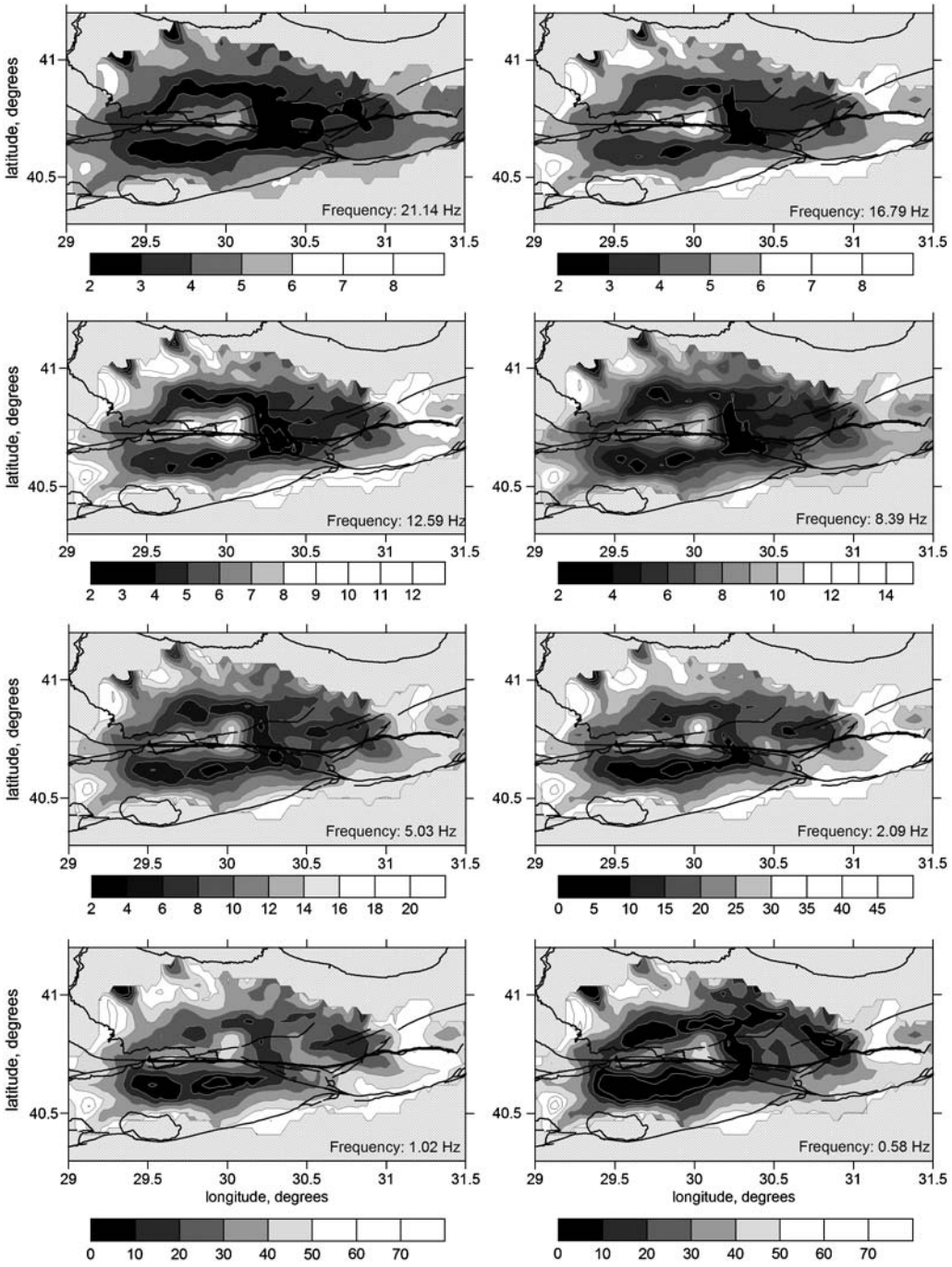

Figure 15. Comparison of the results of attenuation tomography at 10 km depth for eight different frequencies. Indications are the same as in Figure 13. Attenuation ranges, $1/Q_S \times 1000$, are indicated for each plot. Ⓔ A color version of this figure is available in the electronic edition of *BSSA*.

simplified 2D tomographic approach. The tomographic images obtained by higher frequencies also show more localized attenuation heterogeneities than those obtained by lower frequencies. Because this effect cannot be due to different spatial resolution (the ray coverage is the same when inverting for different frequencies), it clearly shows the benefit of performing the inversion using t^* calculated for different frequencies allowing, like in optics, the focus to be tuned on the size of the anomalies of interest.

Finally, we offer some recommendations to other authors for performing similar experiments in the future. The biggest problem of this study was the quite poor spatial resolution in the tomographic inversion caused by poor ray coverage, despite the quite large number of rays and events. This problem is mostly due to the generally accepted practice in tomography studies where only events located inside the network (the GAP criterion) are selected for tomography. Following such a practice leads to many events located

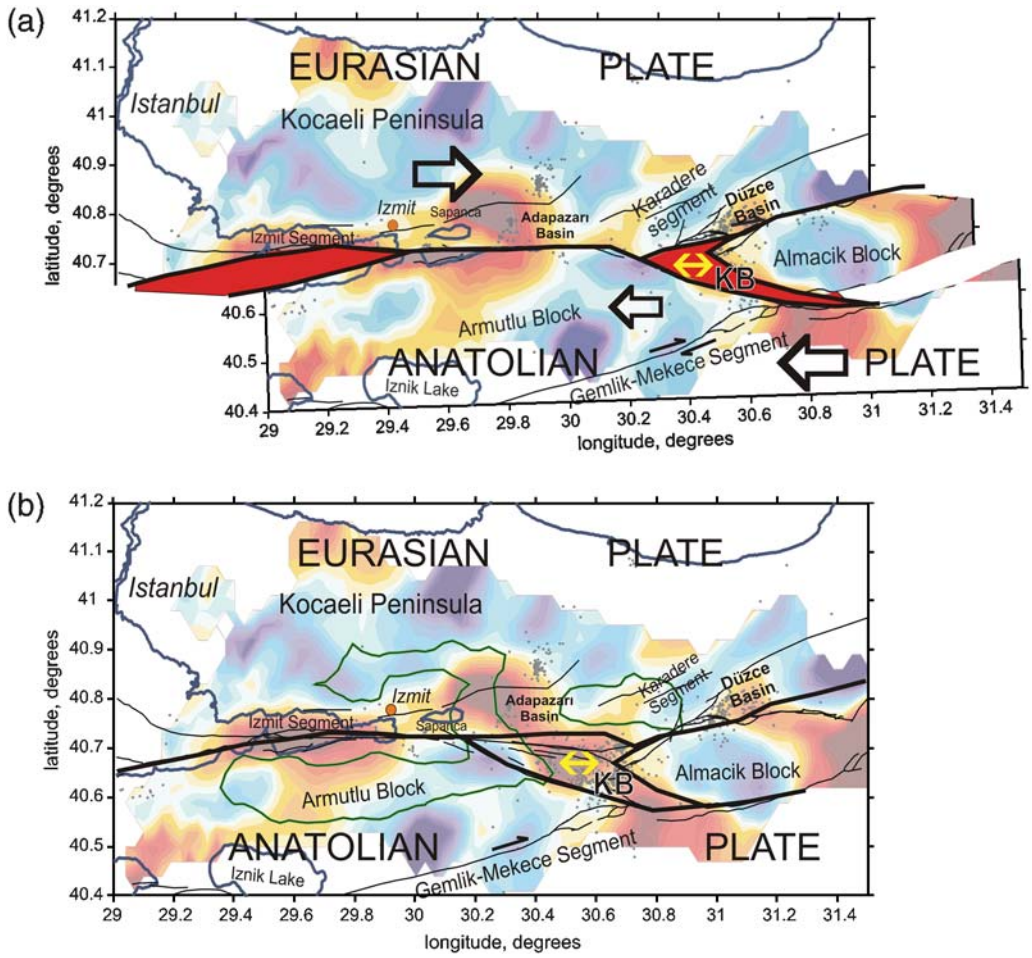

Figure 16. Cartoons for interpretation of the results obtained in this study. (a) Possible reconstruction of the block configuration corresponding to the time of 2 m.y.a. (b) Present day configuration of the blocks. The green line corresponds to the contour line of attenuation $1/Q_S = 15 \times 10^3$ at 10 km depth corresponding to a frequency of 2.09 Hz (Fig. 13). The background is the resulting S-velocity anomalies, the same as in Figure 5. KB is the Kuzuluk basin. The yellow arrows indicate a pull-apart extension in Kuzuluk basin due to right-lateral displacement along the NAFZ. Details of this reconstruction are presented in the text.

outside the network being ignored. Koulakov (2009b) has shown that using the GAP criterion limits considerably the resolution of a tomographic inversion and may actually be detrimental to the quality of the results. We are quite sure that much better vertical and horizontal resolution would be obtained if we used the picks from out-of-network events (at least up to a distance of 400–500 km from the network). We advise all specialists who will perform similar studies to use as much data as possible, including picks from out-of-network sources.

Data and Resources

In this article we present data described in detail in Baumbach *et al.* (2003). The LOTOS code for the tomographic inversion, which is used in this study, is freely available online at www.ivan-art.com/science/LOTOS (last accessed March 2009). This Internet site provides an executable version of the code, its detailed description, manuals, examples of observed and synthetic data sets, and other necessary information.

Acknowledgments

We are grateful to Stefanie Donner for her help in the accurate phase picking. This study would be not possible without the great contribution of S. Zünbül, S. Karakisa, and other Turkish colleagues who took part in the organization and deployment of the networks. We are grateful to Kevin Michael Fleming and Lorraine Wolf for help with manuscript editing. The work of Ivan Koulakov is supported by the Russian Foundation for Basic Researches (08-05-00276-a), Heimholtz Society, and RFBR joint research project 09-05-91321-SIG_a, multidisciplinary project SB RAS 44, and project ONZ RAS 7.4.

References

Adatepe, F., S. Demirel, and B. Alpar (2002). Tectonic setting of the southern Marmara Sea region based on seismic reflection data and gravity modelling, *Marine Geol.* **190,** 383–395.

Aktar, M., C. Dorbath, and E. Arpat (2004). The seismic velocity and fault structure of the Erzincan basin, Turkey, using local earthquake tomography, *Geophys. J. Int.* **156,** no. 3, 497–505.

Ambraseys, N. N., and J. A. Jackson (2000). Seismicity of the Sea of Marmara (Turkey) since 1500, *Geophys. J. Int.* **141,** F1–F6.

Andrews, D. J. (1986). Objective determination of source parameters and similarity of earthquakes of different size, in *Earthquake Source Mechanics*, S. Das, J. Boatwright, and C. H. Scholz (Editors), American Geophysical Monograph **37,** 259–267.

Armijo, R., B. Meyer, A. Hubert, and A. Barka (1999). Westward propagation of the North Anatolian fault into the northern Aegean: Timing and kinematics, *Geology* **27,** 267–270.

Armijo, R, B. Meyer, S. Navarro, G. King, and A. Barka (2002). Asymmetric slip portioning in the Sea of Marmara pull-apart: A clue to propagation process of the North Anatolian fault?, *Terra Nova* **14,** 80–86.

Baris, S., J. Nakajima, A. Hasegawa, Y. Honkura, A. Ito, and S. B. Üçer (2005). Three-dimensional structure of V_P, V_S, and V_P/V_S in the upper crust of the Marmara region, NW Turkey, *Earth Planets Space* **57,** no. 11, 1019–1038.

Barka, A. (1992). The North Anatolian fault, *Ann. Tecton.* **6,** 164–195.

Barka, A., H. S. Akyüz, E. Altunel, G. Sunal, Z. Çakir, A. Dikbas, B. Yerli, R. Armijo, B. Meyer, J. B. de Chabalier, T. Rockwell, J. R. Dolan, R. Hartleb, T. Dawson, S. Christofferson, A. Tucker, T. Fumal, R. Langridge, H. Stenner, W. Lettis, J. Bachhuber, and W. Page (2002). The surface rupture and slip distribution of the 17 August 1999 İzmit earthquake (M 7.4), North Anatolian fault, *Bull. Seismol. Soc. Am.* **92,** 43–60.

Barka, A. A. (1996). Slip distribution along the North Anatolian fault associated with the large earthquakes of the period 1939 to 1967, *Bull. Seismol. Soc. Am.* **86,** no. 5, 1238–1254.

Barka, A. A. (1999). The 17 August 1999 Izmit earthquake, *Science* **285,** no. 5435, 1858–1859

Barka, A. A., and R. Reilinger (1997). Active tectonics of the eastern Mediterranean region deduced from GPS, neotectonic, and seismicity data, *Ann. Geofis.* **40,** 587–610.

Baumbach, M., D. Bindi, H. Grosser, C. Milkereit, S. Parolai, R. Wang, S. Karakisa, S. Zünbül, and J. Zschau (2003). Calibration of an ML scale in northwestern Turkey from 1999 Izmit aftershocks, *Bull. Seismol. Soc. Am.* **93,** no. 5, 2289–2295.

Belin, B., T. Yalçin, F. Suner, E. Bozkurtoglu, A. Gelir, and H. Güven (2002). Earthquake-related chemical and radioactivity changes of thermal water in Kuzuluk-Adapazari, Turkey, *J. Env. Radioact.* **63,** no. 3, 239–249.

Bindi, D., S. Parolai, H. Grosser, C. Milkereit, and S. Karakisa (2006). Crustal attenuation characteristics in northwestern Turkey in the range from 1 to 10 Hz, *Bull. Seismol. Soc. Am.* **96,** no. 1, 200–214.

Bindi, D., S. Parolai, H. Grosser, C. Milkereit, and S. Zümbul (2006). Cumulative attenuation along source-to-receiver paths in northwestern Turkey, *Bull. Seismol. Soc. Am.* **96,** no. 1, 188–199, doi 10.1785/0120050037.

Bouchon, M., and H. Karabulut (2008). The aftershock signature of supershear earthquakes, *Science* **320,** no. 5881, 1323–1325, doi 10.1126/science.1155030.

Carton, H., S. C. Singh, A. Hirn, S. Bazin, B. de Voogd, A. Vigner, A. Ricolleau, S. Cetin, N. Oçakoğlu, F. Karakoc, and V. Sevilgen (2007). Seismic imaging of the three-dimensional architecture of the Cınarcık basin along the North Anatolian fault, *J. Geophys. Res.* **112,** B06101, doi 10.1029/2006JB004548.

Castro, R. R., J. G. Anderson, and S. K. Singh (1990). Site response, attenuation and source spectra of *S* waves along the Guerrero, Mexico, subduction zone, *Bull. Seismol. Soc. Am.* **80,** 1481–1503.

Demirbag, E., C. Rangin, X. Le Pichon, and A. M. C. Sengor (2003). Investigation of the tectonics of the Main Marmara fault by means of deep-towed seismic data, *Tectonophysics* **361,** 1–19.

Greber, E. (1994). Deep circulation of CO2-rich paleowaters in deep seismically active zone (Kuzuluk/Adapazarı, northwestern Turkey), *Geothermics* **23,** 151–174.

Honkura, Y., and A. M. Isikara (1991). Multidisciplinary research on fault activity in the western part of the North Anatolian fault zone, *Tectonophysics* **193,** 347–357.

Honkura, Y., A. M. Işikara, D. Kolçak, N. Orbay, S. Sipahioglu, N. Ohshiman, and H. Tanaka (1985). Magnetic anomalies and low ground resistivity as possible indicators of active fault location: Preliminary results of electric and magnetic observations from the western part of the North Anatolian fault zone, *J. Geomagn. Geoelectr.* **37,** 169–187.

Honkura, Y., A. M. Işikara, N. Oshiman, A. Ito, B. Üçer, Ş. Baris, M. K. Tunçer, M. Matsushima, R. Pektaş, C. Çelik, S. B. Tank, F. Takahashi, R. Yoshimura, Y. Ikeda, and T. Komut (2000). Preliminary results of multidisciplinary observations before, during and after the Kocaeli (Izmit) earthquake in the western part of the North Anatolian fault zone, *Earth Planets Space* **52,** 293–298.

Kanamori, H. (1967). Spectrum of short period core phases in relation to attenuation in the mantle, *J. Geophys. Res.* **72,** no. 1967, 2181–2186.

Karabulut, H., S. Özalaybey, T. Taymaz, M. Aktar, O. Selvi, and A. Kocaoğlu (2003). A tomographic image of the shallow crustal structure in the Eastern Marmara, *Geophys. Res. Lett.* **30,** no. 24, 2277, doi 10.1029/2003GL018074.

Koulakov, I. (2009a). LOTOS code for local earthquake tomographic inversion. Benchmarks for testing tomographic algorithms, *Bull. Seismol. Soc. Am* **99,** no. 1, 194–214, doi 10.1785/0120080013.

Koulakov, I. (2009b). Out-of-network events can be of great importance for improving results of local earthquake tomography, *Bull. Seismol. Soc. Am* **99,** no. 4, 2556–2563, doi 10.1785/0120080365.

Koulakov, I., M. Bohm, G. Asch, B. Luehr, A. Manzanares, K. Brotopuspito, P. Fauzi, M. Purbawinata, N. Puspito, A. Ratdomopurbo, H. Kopp, W. Rabbel, and E. Shevkunova (2007). *P* and *S* velocity structure of the crust and the upper mantle beneath Central Java from local tomography inversion, *J. Geophys. Res.* **112,** B08310, doi 10.1029/2006JB004712.

Koulakov, I., S. V. Sobolev, and G. Asch (2006). *P*- and *S*-velocity images of the lithosphere–asthenosphere system in the Central Andes from local-source tomographic inversion, *Geophys. J. Int.* **167,** 106–126.

Koulakov, I., T. Yudistira, B.-G. Luehr, and Wandono (2009). *P*, *S* velocity and V_P/V_S ratio beneath the Toba caldera complex (Northern Sumatra) from local earthquake tomography, *Geophys. J. Int.* **177,** no. 3, 1121–1139, doi 10.1111/j.1365-246X.2009.04114.x.

Nakamura, A., A. Hasegawa, A. Ito, S. B. Ucer, Ş. Baris, Y. Honkura, T. Kono, S. Hori, R. Pektas, T. Komut, C. Celik, and A. M. Isikara (2002). *P*-wave velocity structure of the crust and its relationship to the occurrence of the 1999 Izmit, Turkey, earthquake and aftershocks, *Bull. Seismol. Soc. Am.* **92,** 330–338.

Okay, A. I., A. Kaslilar-Ozcan, C. Imren, A. Boztepe-Güney, E. Demirbăg, and I. Kuscu (2000). Active faults and evolving strike-slip basins in the Marmara Sea, northwest Turkey: A multichannel seismic reflection study, *Tectonophysics* **321,** 189–218.

Oral, B., R. Reilinger, M. N. Toksoz, R. W. King, A. Barka, I. Kinik, and O. Lenk (1995). Global Positioning System offers evidence of plate motion in Eastern Mediterranean, *EOS Trans. Am. Geophys. Union* **76,** no. 2, 9–11.

Paige, C. C., and M. A. Saunders (1982). LSQR, An algorithm for sparse linear equations and sparse least squares, *ACM Trans. Math. Soft.* **8,** 43–71.

Parolai, S., D. Bindi, E. Durukal, H. Grosser, and C. Milkereit (2007). Source parameters and seismic moment-magnitude scaling for northwestern Turkey, *Bull. Seismol. Soc. Am.* **97,** no. 2, 655–660.

Pondard, N., R. Armijo, G. C. P. King, B. Meyer, and F. Flerit (2007). Fault interactions in the Sea of Marmara pull-apart (North Anatolian fault): Earthquake clustering and propagating earthquake sequences, *Geophys. J. Int.* **171,** 1185–1197.

Salah, M. K., S. Sahin, and M. Kaplan (2007). Seismic velocity structure along the western segment of the North Anatolian fault zone imaged by seismic tomography, *Bull. Earthq. Res. Inst. Univ. Tokyo* **82,** 209–223.

Smith, A. D., T. Taymaz, F. Oktay, H. Yuce, B. Alpar, H. Basaran, A. J. Jackson, S. Kara, and U. Simsek (1995). High resolution seismic profiling in the Sea of Marmara (NW Turkey): Late Quaternary

sedimentation and sea level changes, *Geol. Soc. Am. Bull.* **107,** no. 8, 923–936.

Straub, C., and H. G. Kahle (1994). Global Positioning System (GPS) estimates of crustal deformation in the Marmara Sea region, Northwestern Anatolia, *Earth Planet. Sci. Lett.* **121,** 495–502.

Tibi, R., G. Bock, Y. Xia, M. Baumbach, H. Grosser, C. Milkereit, S. Karakisa, S. Zübül, R. Kind, and J. Zschau (2001). Rupture processes of the August 17 İzmit and November 12, 1999, Düzce (Turkey) earthquakes, *Geophys. J. Int.* **144,** no. 2, F1–F7.

Van der Sluis, A., and H. A. van der Vorst (1987). Numerical solution of large, sparse linear algebraic systems arising from tomographic problems, in *Seismic Tomography*, G. Nolet (Editor), Reidel, Dortrecht, 49–83.

Yaltirak, C. (2002). Tectonic evolution of the Marmara Sea and its surroundings, *Mar. Geol.* **190,** 493–529.

Yaltirak, C., and B. Alpar (2002). Evolution of the middle strand of North Anatolian fault and shallow seismic investigation of the southeastern Marmara Sea (Gemlik Bay), *Marine Geol.* **190,** no. 1–2, 307–327.

Yilmaz, Y., S. C. Genc, E. Yigitbas, M. Bozcu, and K. Yilmaz (1995). Geological evolution of the late Mesozoic continental margin of Northwestern Anatolia, *Tectonophysics* **243,** 155–171.

Institute of Petroleum Geology and Geophysics
SB RAS, Prospekt Akademika Koptuga, 3
Novosibirsk, 630090, Russia
KoulakovIY@ipgg.nsc.ru
(I.K.)

Istituto Nazionale di Geofisica e Volcanologia
Via Bassini, 15
20133 Milano, Italy
(D.B.)

Helmholtz Centre Potsdam
GFZ German Research Centre for Geosciences
Telegrafenberg, 14473
Potsdam, Germany
(S.P., H.G., C.M.)

Manuscript received 27 April 2009